

Sequential growth of deformation bands in a multilayer sequence

Christian Klimczak,^{1,2} Roger Soliva,⁴ Richard A. Schultz,^{1,3} and Jean Chéry⁴

Received 14 March 2011; revised 16 June 2011; accepted 28 June 2011; published 28 September 2011.

[1] The outstanding exposure of deformation bands in a multilayer sequence of the Orange quarry, Provence, France, motivates a study investigating the development and controls of deformation band geometries by field mapping combined with finite element modeling. Field mapping yields new insights into angular relations between, and evolution of, the deformation bands as well as provides input parameters for the setup and boundary conditions of the numerical simulations using ADELI 2D. In particular, reverse-sense deformation bands are found to have developed within three of the four exposed layers of the multilayer stack with similar orientations to bedding, indicating layer-parallel contraction. Numerical simulations, carried out as a parametric study to investigate the influence on deformation band development and geometry, successfully reproduce the sequential development of deformation bands in the three layers as seen in the field as well as recreate the observed angular geometries of $\sim 39^\circ$ to the maximum compression. This angular relationship is put into context with observations from other field studies and theoretical values to explore controls of deformation band orientations. Furthermore, band localization is impeded in the model by increased layer cohesive strength, demonstrating the importance of host-rock property variations on where localization of bands within the multilayer sequence. Results from both field investigation and numerical simulations are consistent with regional tectonics, where the strata underwent gentle folding due to thrust faulting at depth, and bring further insight into the development and geometry of deformation bands in both extensional and contractional tectonic regimes.

Citation: Klimczak, C., R. Soliva, R. A. Schultz, and J. Chéry (2011), Sequential growth of deformation bands in a multilayer sequence, *J. Geophys. Res.*, 116, B09209, doi:10.1029/2011JB008365.

1. Introduction

[2] Prior to faulting, strain in porous rock is accommodated by the concentration of shearing and compactional deformation in well-defined zones, referred to as deformation bands. Most deformation bands reduce the porosity of the host rock, display a continuous change in strength or stiffness across a relatively narrow zone, and form networks with distinct band geometries. These band characteristics highly affect the hydro- and rock mechanical properties of the host rock, so that understanding the controls of development of deformation bands and their network geometries is central to characterizing the mechanics and evolution of brittle deformation in granular rock and evaluating the quality of reservoirs. For example, knowledge of the controls on band geometries helps further define fluid migration pathways

because of the role of deformation and compaction bands as barriers and baffles [e.g., *Fossen et al.*, 2007] or conduits [*Du Bernard et al.*, 2002a] for fluid flow [*Fossen and Bale*, 2007; *Sternlof et al.*, 2006].

[3] In the Orange quarry in the Bassin du Sud-Est, France, a systematic network of prominent deformation bands [*Saillet and Wibberley*, 2010] is exposed in an arenitic sandstone layer, bounded by calcite cemented sandstone layers both containing fewer or no deformation bands. The different properties of the layers with differing intensities of deformation allow the extraction of a variety of information on rock properties as well as geometry and kinematics of the band network, making the exposure of this multilayer sequence ideal for studying the lithological and structural controls on deformation band development.

[4] In this paper, we investigate rheological, structural, and mechanical controls of deformation band geometries and network evolution by pairing a detailed field study at the Orange quarry with finite element simulations of band growth. This study aims to further understand the effects of rock properties on angular relationships of deformation bands with respect to the principal stress axes. Results from the field are presented and then translated into a numerical model in order to detect the controls that govern the formation of the observed deformation band geometries. Our results have implications for the formation of deformation

¹Geomechanics-Rock Fracture Group, Department of Geological Sciences and Engineering, University of Nevada, Reno, Reno, Nevada, USA.

²Now at Department of Terrestrial Magnetism, Carnegie Institution of Washington, Washington, D. C., USA.

³Now at ConocoPhillips, Houston, Texas, USA.

⁴Géosciences, Université Montpellier II, Montpellier, France.

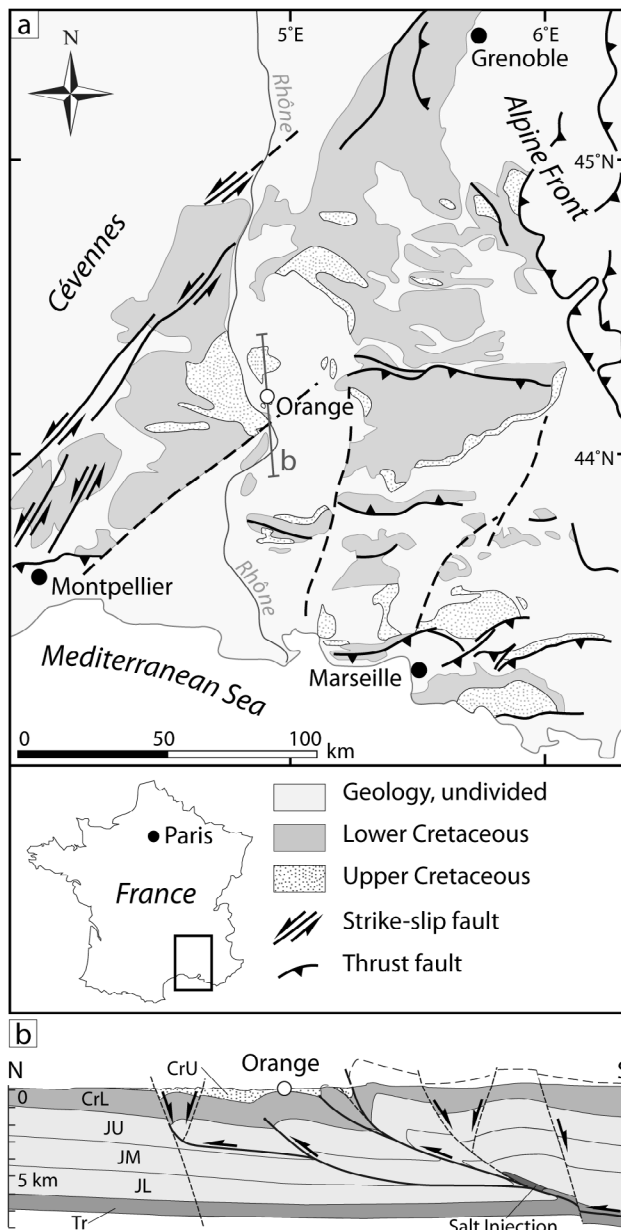


Figure 1. Geologic context of the Bassin du Sud-Est, Provence, France. (a) Geologic map of the Bassin du Sud-Est. The Orange exposure is located in the central basin. (b) Cross section from north to south through the central Bassin du Sud-Est. Orange is located on a gentle anticline, which developed over thrusting at depth. CrU, Upper Cretaceous; CrL, Lower Cretaceous; JU, Upper Jurassic; JM, Middle Jurassic; JL, Lower Jurassic; Tr, Triassic.

band networks on plastic yield surfaces as well as for the regional tectonic evolution in the Bassin du Sud-Est.

2. Background

[5] In granular rock or soils, deformation is commonly characterized from a critical-state soil plasticity perspective. In such materials deformation causes dilation, compaction, or shearing by changing the grain packing or mechanically

reducing grain sizes, which leads to yielding. Yielding, the transition from elastic to plastic deformation [e.g., Rudnicki, 1977], describes the onset of compactional shear band formation, which is represented on an elliptical or teardrop-shaped yield envelope [e.g., Wong and Baud, 1999; Olsson, 1999; Rudnicki, 2004; Schultz and Siddharthan, 2005; Grueschow and Rudnicki, 2005; Wibberley et al., 2007]. The shape of the yield envelope, which is plotted in q - p diagrams with q representing the shear stress and p the mean stress, is characterized by a positive slope at lower mean stresses and a negative slope, referred to as a cap, at higher mean stresses. Deformation occurring on the positive-slope side is commonly associated with volume increase and includes dilational shear bands as well as bands with discrete slip surfaces and faults [e.g., Schultz and Siddharthan, 2005; Wibberley et al., 2007; Sallet and Wibberley, 2010], whereas the cap side of the envelope is typically associated with volume decrease showing compactional deformation, such as compactional shear bands [Wong and Baud, 1999; Olsson, 1999; Rudnicki, 2004; Karner et al., 2005; Schultz and Siddharthan, 2005; Grueschow and Rudnicki, 2005; Wibberley et al., 2007; Sallet and Wibberley, 2010].

[6] Laboratory testing, mostly performed under triaxial compression, has involved monitoring of acoustic emission, failure modes, spatial distribution of damage and evolution of deformation band localization in order to better understand compactional deformation localization in granular rock [e.g., Zhang et al., 1990; Saada et al., 1999; Wong and Baud, 1999; Baud et al., 2004; Karner et al., 2005; Stanchits et al., 2009; Lothe et al., 2002; Mair et al., 2000]. By testing a variety of different sandstones, Baud et al. [2004] observe a broad spectrum of geometric complexity of bands and distinguish between two end-members, conjugate shear bands with angles to the maximum compression of 45° to 80° and discrete compaction bands, perpendicular to the maximum compression. With similar band geometries, Mair et al. [2000] present laboratory evidence for a sequential growth of discrete deformation bands.

[7] Angular relations were specifically studied by triaxial testing [Olsson, 1999] and also by field observations [Olsson et al., 2004; Eichhubl et al., 2010; Schultz et al., 2010]. Results indicate that, in contrast to faults, compaction bands (referred to as either pure or shear-enhanced compaction bands in the literature [e.g., Eichhubl et al., 2010]) form with outer-normal angles to the maximum compressive stress of less than 45°. However, deformation bands that accommodate predominantly shearing strains such as the classic cataclastic bands studied by Aydin [1978], Aydin and Johnson [1978], Fossen and Hesthammer [1997], Shipton and Cowie [2001, 2003], Wibberley et al. [2007], and Sallet and Wibberley [2010], which are also associated with yielding on a yield surface, form with fault-like outer-normal angles of more than 45° to the principal axis of maximum compression, evident from both the field [Johnson, 1995; Davis et al., 2000; Olsson et al., 2004] and laboratory testing [Ord et al., 1991]. This apparently disparate behavior between the two types of bands is interesting and is explored in this paper.

[8] A network of reverse-sense deformation bands [Sallet and Wibberley, 2010] is spectacularly exposed in the Orange quarry in the central Bassin du Sud-Est, France (Figure 1). The Bassin du Sud-Est is a sedimentary basin bordered by

the Alps to the northeast, the Cévennes to the northwest and the Mediterranean Sea to the south (Figure 1a). The surface geology is dominated by Lower and Upper Cretaceous limestone and sandstone layers, which were deformed during three major tectonic events. The basin was first affected by Late Cretaceous Eoalpine and especially Pyrenean shortening, accomplished by the inversion of pre-existing normal faults faulting and folding of the Mesozoic strata [Arthaud and Séguret, 1981; Tempier, 1987; Séranne et al., 1995; Séguret et al., 1996; Sanchis and Séranne, 2000] (Figure 1b). Oligocene opening of the Gulf of Lion and related Miocene compression caused normal faulting and strike-slip reactivation of the pre-existing faults, respectively [Roure et al., 1994; Séranne et al., 1995; Ford and Stahel, 1995; Sallet and Wibberley, 2010].

[9] The deformation bands in the Orange quarry are reported to occur in a distributed, conjugate reverse-sense array of two low angle ESE-WNW striking sets of cataclastic bands [Sallet and Wibberley, 2010]. In order to formulate a general model for deformation band distribution and network evolution, Sallet and Wibberley [2010] statistically evaluated this and other nearby networks with a quantitative examination of bands along scan lines. Their resultant deformation band frequency distribution led to an interpretation of the network evolution with an overall homogenous bulk strain but a heterogeneous density distribution of the individual sets.

[10] While field observations indicate that deformation bands from extensional tectonic settings localize and cluster in narrow zones surrounding discrete fault planes [e.g., Johnson, 1995; Davis, 1999; Du Bernard et al., 2002b; Shipton et al., 2002; Sallet and Wibberley, 2010], distributed deformation band networks, such as the one reported from the Orange quarry [Sallet and Wibberley, 2010], are associated with contractional deformation, such as above or adjacent to fault related folds [e.g., Davis, 1999; Cashman and Cashman, 2000]. Such distributed reverse-sense conjugate deformation band networks, where bands are confined to a single layer, are reported from the Colorado Plateau associated with the Rubys Inn thrust [Davis, 1999] or the Subhercynian Cretaceous Basin, Germany, associated with the Northern Harz Mountains Border Fault [Klimczak, 2011]. At both field sites from contractional tectonic settings, the distributed pervasive, rather than clustered, nature of hundreds, if not thousands, of reverse-sense deformation bands is distinctive.

[11] Field-scale geometrical properties of deformation bands are commonly documented and interpreted in terms of their relation to nearby faults [e.g., Hesthammer and Fossen, 2001; Shipton and Cowie, 2001, 2003; Du Bernard et al., 2002b; Okubo and Schultz, 2005], where it is found that geometry and intensity of individual deformation bands and the deformation band damage zone depend on the proximity to the main fault. Furthermore, evaluations of the overall stress field leading to conjugate arrays [e.g., Olsson et al., 2004] and stress orientations between overlapping bands leading to ladder structures [Schultz and Balasko, 2003; Okubo and Schultz, 2006] resulted in mechanical models of band propagation and interaction that were able to explain the observed geometries.

[12] The development of widespread distributed deformation band networks confined to a single layer, as opposed

to narrow deformation band clustering around faults, can affect fluid flow through and engineering properties of the host rock, such as rock strength and stiffness, on the aquifer and reservoir scales. Therefore, information on the distribution and geometry of such band networks provides important input parameters for numerical models [e.g., Kolyukhin et al., 2010] and is useful for the exploration and extraction of hydrocarbons and groundwater.

3. Field Results

[13] The Orange quarry, located in the central western part of the Bassin du Sud-Est (Figure 1a), displays a shallowly southward dipping, multilayered sequence of Cenomanian sandstones and marls that occur in the hinge region of a very gentle fold related to thrusting at depth (Figure 1b). Four major layers are exposed (Figure 2a). The contacts between the layers are generally planar, however, undulations between the individual layers and variations in layer thickness occur locally. The nature of all contacts is depositional, with no evidence for shearing or opening along layer contacts. Layer 1, the lowermost of the exposed layers, consists of a well-cemented, cross bedded arenitic sandstone. It is overlain by layer 2, which is ~14 m thick and composed of a poorly cemented, highly porous, homogenous quartz arenite. The overlying layer 3 is very heterogeneous; it is comprised of alternating beds of marly limestones and calcite cemented sandstones. This layer is at least 10 m thick and can locally contain intercalated beds of the overlying layer 4. Layer 4 is similar in properties to layer 2, but is, in places, observed to be better cemented. Total thicknesses of layers 1 and 4 are unknown, due to lack of exposure.

[14] Two sets of prominent, multiple-strand, cataclastic deformation bands occur in layer 2 [Wibberley et al., 2000; Sallet and Wibberley, 2010] (Figures 2a and 2b). The distribution of bands throughout this layer is continuous and at consistently high density, with systematic variations in band density between the individual north-dipping and south-dipping sets [Sallet and Wibberley, 2010]. The bands of layer 2 also continue into layer 1, in which they become less prominently developed. Layer 3 is completely devoid of bands, whereas layer 4 displays bands. Compared to the bands of layer 2, bands of layer 1 are less prominently developed in terms of both number and thickness of bands. Bands of layer 4 are similarly developed and, in places, even more closely spaced than in layer 2. Exposure of both layers 1 and 4 is incomplete due to partial burial or erosion so that analysis of band geometry, as done for bands of layer 2, was not performed.

[15] Reexamination of the deformation band network in layer 2 (Figure 2) and mapping of the entire exposure (Figure 3) reveal a total of four sequential sets of reverse-sense deformation bands (Figure 2c). In particular, there are two generations each of northward and southward dipping sets. For both generations the southward-dipping set pre-dates the northward-dipping set (Figure 2c), so that the chronologic order, in which the bands formed, from oldest to youngest is: first generation southward dipping bands (S1), first generation northward dipping bands (N1), second generation southward dipping bands (S2) and second generation northward dipping bands (N2) (Figures 2c, 2f, 2g, and 3a).

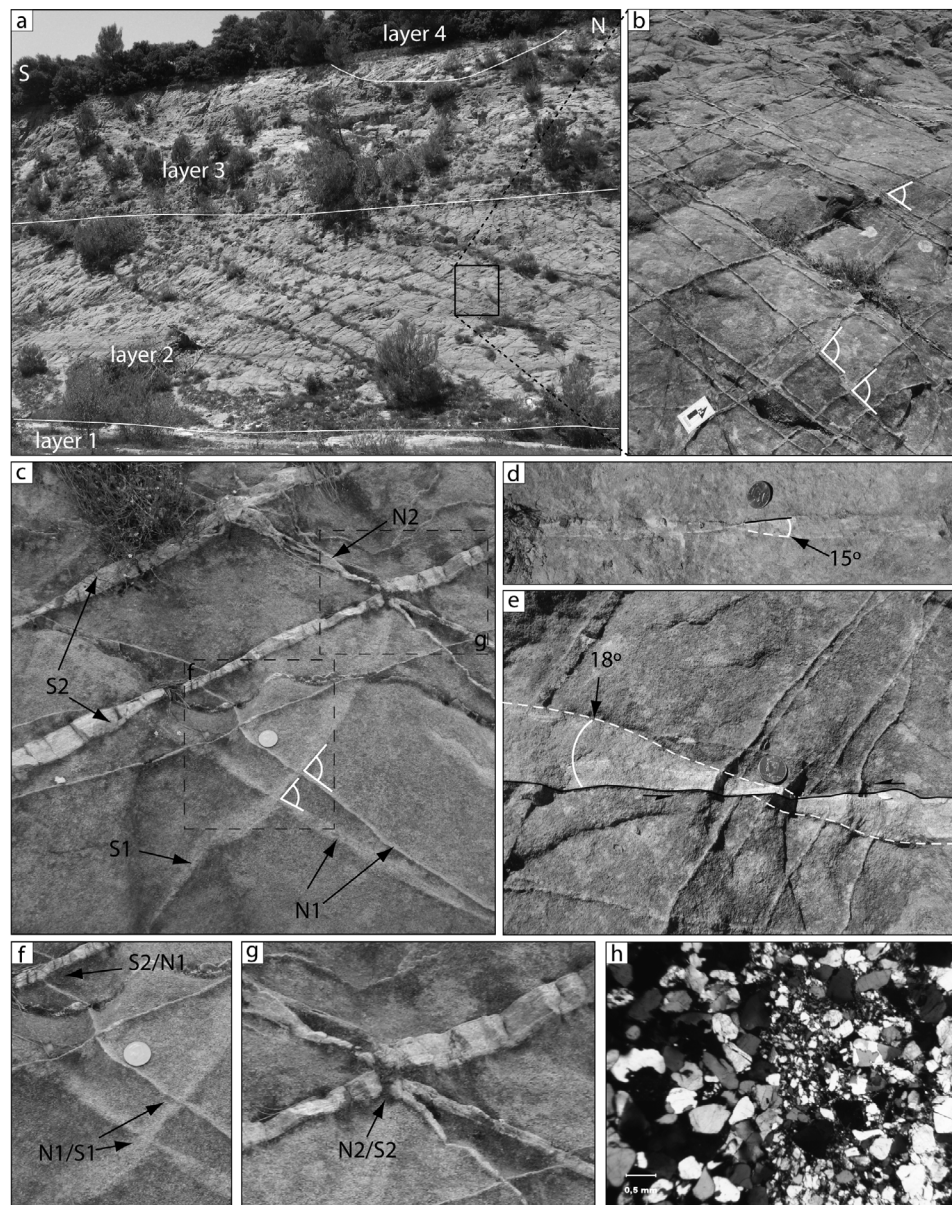


Figure 2. Deformation as seen in the Orange quarry. (a) Overall appearance of the four layers of the exposure as well as preferential development of deformation bands in layer 2. (b) Detailed view of the deformation band geometry in layer 2. Bands of the second generation only are exposed. (c) Deformation bands of the four different sets sequentially crosscutting each other. (d) Isolated multiple strand deformation band displaying a twisted ribbon structure. (e) Multiple-strand twisted ribbon band crosscutting several bands of a previous set. (f) Band intersections of N1 bands crosscutting S1 bands as well as S2 bands crosscutting N1 bands. (g) Band intersection of N2 bands cutting S2 bands. (h) Cross-polarized photomicrograph of first generation deformation band showing cataclasis.

[16] In the field, the bands of the two generations are distinguishable from each other by the amount of shear across the bands, difference in color, and resistance to weathering and erosion (Figure 2c). The older bands are light gray, show small amounts of shear across them relative to their thickness, and do not display a positive morphological relief as compared to the host rock. The two sets of bands of the second generation are of beige to light brown colors, weather out of the host rock with positive relief, and display shear

across them equaling or exceeding their band thickness. Bands of the second generation are developed as multiple strands of cataclastic bands [Saillet and Wibberley, 2010], whereas bands of the first generation form as thick single strands also showing a cataclastic texture (Figure 2h).

[17] Many bands, especially of the second generation, display a twisted ribbon structure (Figures 2d and 2e). A twisted ribbon is characterized by a change in orientation of the individual strands of a multiple strand deformation band. Due

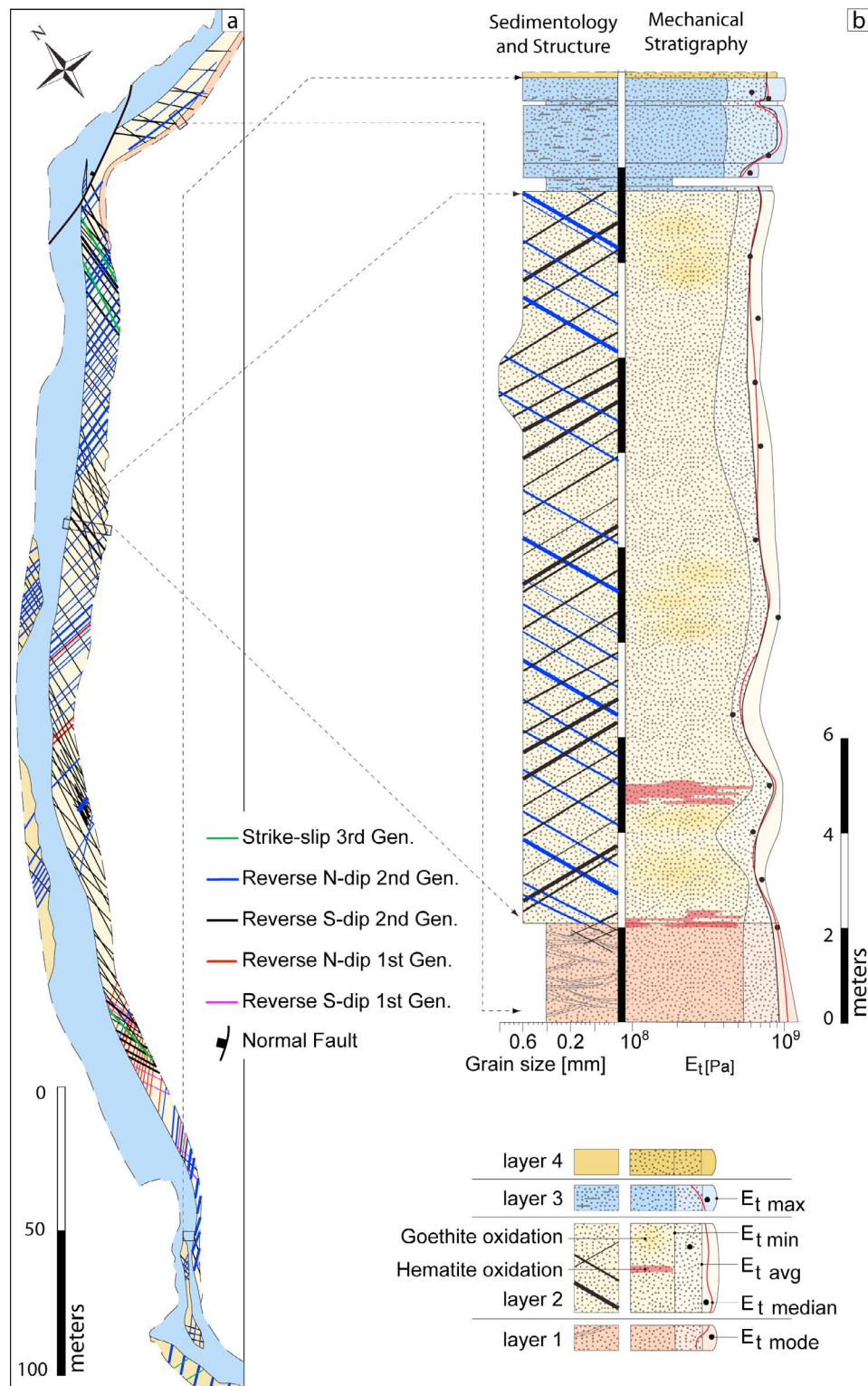


Figure 3. Geologic map and stratigraphic section of the strata exposed in the Orange quarry. (a) Map of the exposure of the Orange quarry. Four layers of Upper Cretaceous sandstones and limestones are deformed, where deformation bands are prominently developed in layer 2. Thick, multiple strand bands were individually mapped. Bands of the different sets are shown in different colors. Band thickness is indicated by line thickness. (b) Stratigraphic column showing grain size and sedimentological characteristics of the accessible layers as well as mechanical layering. Layers 1 and 2 are fairly homogenous, layer 3 is very heterogeneous, layer 4 is inaccessible. Tangent Young's modulus (E_t), calculated from Schmidt hammer rebound values, shows little variation throughout the layers.

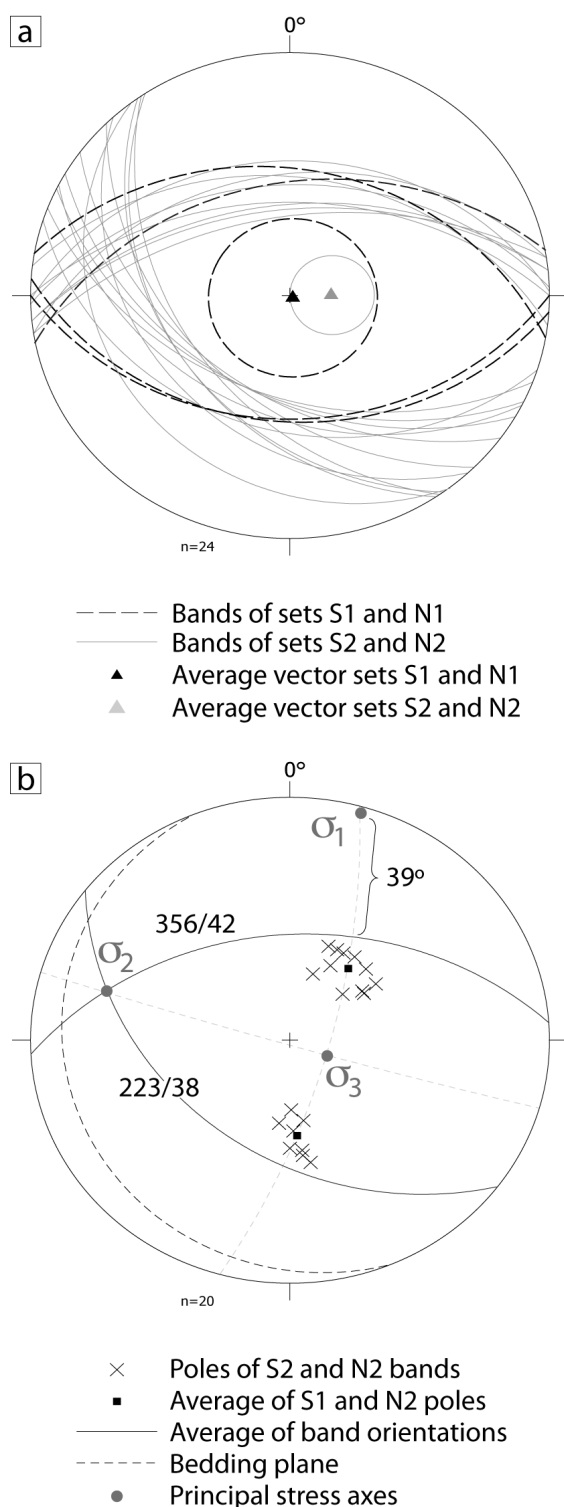


Figure 4. Equal-area plot for the determination of the stress field in which the deformation bands formed. (a) Equal-area plot of deformation band orientations of the different generations. Their average vectors are plotted with 95% ellipse. The ellipses of the two generations match, indicating that both generations formed in the same stress field. (b) Determination of the principal stress axes. The maximum compressive principal stress (σ_1) acts on a subhorizontal plane, approximately parallel to bedding.

to that orientation change, each newly formed strand cuts through the previously formed strands. The intersection along the band is usually confined to a single point (Figure 2d) or a narrow zone (Figure 2e). The latest strand of the twisted ribbon forms usually the most prominent strand along which the most offset occurs (Figure 2e). The total change in orientation between the initial and ultimate bands forming the twisted ribbons is usually $\sim 15^\circ$ but is observed to be up to 20° (Figures 2d and 2e). Twisted ribbons can occur isolated (Figure 2d) but mostly the twist region crosscuts through one or more bands of an earlier generation (Figure 2e). Similar bands, described as distinctive braided patterns, are also found in the Navajo Sandstone in southeastern Utah [Davis, 1999].

[18] Orientations of the reverse-sense bands were measured to investigate the geometrical relationships between the bands and to infer the stress field in which the bands formed (Figure 4). Bands of the first generation generally dip to the south or north at 45° (Figure 4a) or higher (Figure 2c). Similar to the findings of Sallet and Wibberley [2010], bands of the second generation dip toward the north and southwest with dips from as low as 18° to up to 50° (Figures 2c and 4a). The mean vectors of the two generations were calculated by adding the unit vectors of each of the two generations of bands. Unit vectors were plotted in their 95% confidence ellipse to identify whether the two generations formed within the same or a temporally varying remote stress field. The 95% confidence ellipse of the second generation bands is completely contained within that of the first generation bands and both average vectors lie within the ellipse of the other generation (Figure 4a). This indicates that bands of both generations have similar orientations so that they are likely to have originated from within the same remote stress field.

[19] Knowing the kinematics of the bands, the direction of the maximum compressive stress was obtained by finding the acute bisector between the bands. The results indicate that the maximum compressive stress (σ_1) is nearly horizontal and acted subparallel to bedding (Figure 4b). The difference between maximum compressive stress and bedding is 6.6° , which is in the range of variation of band dip angles of $\sim 15^\circ$.

[20] The average angle between the maximum compressive stress and the mean orientation of second-generation deformation bands is 39° (Figure 4b). However, dihedral angles between individual bands of sets S2 and N2 vary between 60° and 100° (Figure 2b), so that the angle between the maximum compressive stress and second-generation band orientations can vary between 30° and 50° . The angles between individual bands of the first generation are $\sim 90^\circ$ or greater (Figure 2c) so that angles between the maximum compressive stress and these bands are 45° or more. The average angle of 39° between second-generation bands and maximum compression is consistent with frictional sliding due to the remote stress state, similar to findings for laboratory-scale deformation bands analyzed by Ord et al. [1991] and Olsson et al. [2004]. First-generation bands are developed at angles $> 45^\circ$ to the maximum compression, similar to what is found for shear-enhanced compaction bands in both laboratory and field settings [Olsson, 1999; Eichhubl et al., 2010; Schultz et al., 2010].

[21] The spatial distribution of the different sets of bands throughout the Orange quarry is shown in Figure 3a. In layer 2, S2 and N2 bands occur throughout the entire

exposure, whereas S1 and N1 bands are only developed in the central and predominantly in the southern portion of layer 2. Twisted ribbon bands occur throughout the entire layer. In addition to the sets of reverse-sense bands, a younger, fifth set of deformation bands is present at the outcrop that was previously described to consist of near vertical normal-sense bands [Saillet and Wibberley, 2010]. We suggest that the sense of these bands is better described as strike-slip, because they display lateral offsets despite their near-vertical dip. Only a handful of these bands were observed throughout the entire exposure of layer 2 so that we do not further consider these bands for our study. The northern part of the exposure is cut by a normal fault (Figure 3a), which displays offset in the range of tens of meters [Saillet and Wibberley, 2010].

[22] The reverse-sense deformation bands in layer 2 were previously described as conjugate [Wibberley *et al.*, 2000; Saillet and Wibberley, 2010], implying that they formed contemporaneously in the same stress field [Freund, 1970; Marshak *et al.*, 1982]. Although the bands originated from within the same stress field, our mapping (Figure 3a) shows that, on the scale of the outcrop, the four sets formed sequentially, i.e., one set after another, rather than in a contemporaneous manner. The mapped chronological relationship of the different sets of bands (Figure 3a) holds true for all multiple-strand bands, so that these bands did not form as conjugate arrays.

[23] A stratigraphic profile was taken through the accessible part of the quarry exposure (Figure 3b). A total section of 20 m was measured containing the entire layer 2 and parts of layers 1 and 3. The section was analyzed in terms of grain size, measured with a grain size chart, and sedimentological characteristics as well as variations in the stiffness using an L-type Schmidt hammer (Figure 3b) in order to assess rock and layer properties for use in the finite element modeling.

[24] The grain size analysis shows that the grain size is comparable between and within the layers. Grains have average sizes of 0.6 ± 0.2 mm throughout the entire section (Figure 3b). Layer 2 is fairly homogenous. Layer 1 is comprised of a well-cemented sandstone with slightly lower grain size (~ 0.4 mm) than that of layer 2 (~ 0.6 mm, Figure 3b) and displays prominent long-wavelength, low amplitude cross-bedding structures. Layer 4 shows the greatest variations in both grain size and sedimentary structures. Here, marly limestone units are interbedded with calcareous sandstones, where many shallow marine fossils occur. In addition to the sedimentary structures, iron oxidation horizons occur throughout the layers. They are most prominent in layer 2 (Figure 3b). Oxidations can either be dark rusty red or dark yellow.

[25] In order to assess the stiffnesses of the different layers, values of tangent Young's modulus (E_t) throughout the measured section were computed. The tangent Young's modulus was obtained by converting measured L-type Schmidt hammer rebound values with a standard conversion by Aufmuth [1973] following the ISRM suggested method [Aydin, 2009]. Measurements along the section were taken in intervals of >1 to 2 m and 10 rebound values were measured per station. The resultant values for tangent Young's modulus were then plotted in the mechanical stratigraphy section as a function of its mean, median, mode and range between the minimum and maximum values of the readings (Figure 3b).

[26] The stiffness measurements indicate that there is no significant variation in tangent Young's modulus between the different layers. Layers 1 and 3 have a greater variation than layer 2 but all mean, median, and mode values vary around 0.8 GPa (Figure 3b). Elevated values of rock stiffness are found in the oxidation horizons (Figure 3b). These oxidations originate from fluid migration through the sandstone, since they are enriched in horizons above less permeable sandstone layers and frequently terminate abruptly at deformation bands, highlighting the function of the bands as barriers for fluid flow and showing that the oxidations postdate the formation of the bands. Therefore, the stiffness anomalies caused by the oxidations can be neglected for the assessment of the rock properties that control the development of deformation bands.

4. Modeling

4.1. Modeling Method and Parameters

[27] The finite element software ADELI is used to model the deformation of a multilayer sequence based on the exposure in the Orange quarry. ADELI was designed to model the thermomechanical behavior of the crust and lithosphere at geological timescales using triangular elements for 2-D and tetrahedral elements for 3-D quasi-static problems (J. Chéry and R. Hassani, unpublished ADELI user manual, 2005). Both 2-D and 3-D codes have been successfully used to model the large-scale mechanics of faulting and associated stress or displacement fields [e.g., Hassani and Chéry, 1996; Chéry, 2001; Provost *et al.*, 2003; Chéry *et al.*, 2004; Vernant and Chéry, 2006; Wang *et al.*, 2008]. In this study, outcrop scale deformation in a multilayer sequence was modeled with the 2-D version of ADELI in order to investigate the geometry and evolution of the deformation bands as recorded from the field.

[28] The model contains four layers, by analogy with the exposure of the Orange quarry (Figure 5). The total thickness (d) of the multilayer sequence is chosen to be 64 m, of which layers 1 and 4 were both assigned a thickness of $d = 20$ m and layers 2 and 3 were assigned their average field values of $d = 14$ m and $d = 10$ m, respectively (Figure 5). Layers 1 and 4 constitute the outer layers of the model and are chosen to be the thickest layers of the sequence, so that boundary effects at the upper and lower parts of the model are minimized on layers 2 and 3. The model was assigned a horizontal length (l) of 300 m. This value is similar to the length of the central portion of the Orange quarry (Figure 3a) and is long enough so that edge effects are minimized.

[29] Once the model geometry is set up, the code automatically generates a mesh of specified number of elements and mesh size. The mesh was created with pairs of triangular elements as suggested for elasto-plastic rheologies (J. Chéry and R. Hassani, unpublished ADELI user manual, 2005). Once the mesh is generated, rheological properties and material constants are defined for the individual layers.

[30] The deformation was modeled using an elastic-plastic constitutive relation. We choose the Drucker-Prager criterion, which is a widely used rock failure law to describe pressure-dependent frictional deformation [Davis and Selvadurai, 2002, pp. 65–66] that is similar to the Mohr-Coulomb criterion but more stable in finite element computations [e.g., Schultz-Ela and Walsh, 2002]. For our simulations the input

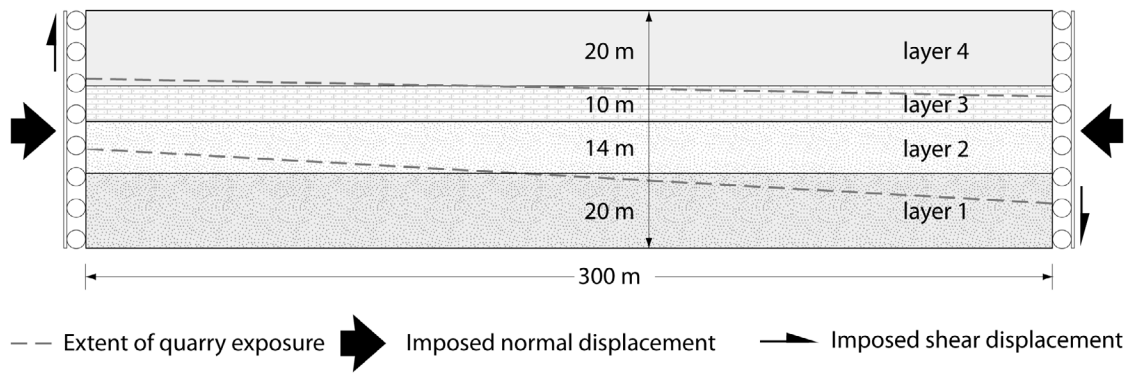


Figure 5. Model setup based on exposure geometry. Boundary conditions are derived from band orientations. Rheological parameters (Drucker-Prager, stiffness) were assigned based on literature values and Schmidt hammer testing.

parameters include tangent Young's modulus (E_t), Poisson's ratio (ν), rock density (ρ), as well as cohesion (C), friction angle (ϕ), and dilatancy angle (ψ). The code allows modeling strain hardening or softening by specifying initial and final friction angles (ϕ_{ini} , ϕ_{fin}) and setting the limit of plastic strain (κ_c). When κ_c is reached, the initial becomes the final friction angle. We find that our results are not sensitive to reasonable variations in these parameters.

[31] Deformation was driven by remote displacements imposed at a given constant rate (Table 1). We evaluated two plausible cases inferred from the field observations: layer-parallel compression (Figure 6a) and maximum compression that was slightly misaligned to the layers (Figures 6b and 6c),

to simulate gentle tilting of the stratigraphic sequence during fault-related folding, as suggested for folding in general by *Suppe* [1983], *Suppe and Medwedeff* [1990], and *Ford and Stahel* [1995] (see Figure 1b).

[32] The effects of variations of principal geometric and rheologic parameters as well as effects of the boundary conditions on the simulations were analyzed in a parametric study. All input parameters for the ADELI 2D simulations in this study, including their effect on the model and implications for the mechanics and development of deformation bands, are listed in Table 1. Input parameters were chosen based on field measurements or estimates from standard values of rock-physical properties, depending on

Table 1. Overview of the Main Variables and Parameters Used for the Numerical Simulations

Symbol	Explanation and Units	Effect on Model	Implications
<i>Material Properties</i>			
E_t	Tangent Young's modulus (Pa)	Number of bands and amount of strain on individual bands	Smaller values promote spatially distributed bands, larger values promote clustering
ν	Poisson's ratio	Not varied	-
ρ	Density (kg/m ³)	Not varied	-
<i>Drucker-Prager Yield Criterion</i>			
C	Cohesion (Pa)	Larger values impede band formation	High cohesion units don't develop clustering
ϕ_{ini}^a	Initial internal friction angle (deg)	Strain accommodated in distributed or localized manners, minor changes in band orientation	Smaller values promote wide zones of non-localized shear
ϕ_{fin}^a	Friction angle after strain softening (deg)	Hard: high ϕ , lock up at band intersections	
κ_c^a	Limit of plastic strain after which $\phi_{ini} = \phi_{fin}$	Soft: low ϕ , distributed bands	
ψ	Dilatancy angle (deg)	Not varied, set to 0.	-
<i>Boundary Conditions and Model Setup</i>			
d	Layer thickness (m)	Lengths of bands	-
l	Model length (m)	Longer model decreases boundary effects	-
V_n	Displacement rate, normal component (m/s)	Magnitude of strain, band geometry unaffected	Promote conjugate sets of bands
V_t	Displacement rate, shear component (m/s)	Preferential development of one set of bands	Promote single sets of bands
x	Mesh size	Band thickness and spacing, and number of bands	-
t	Time steps	-	-

^aAll three variables interact.

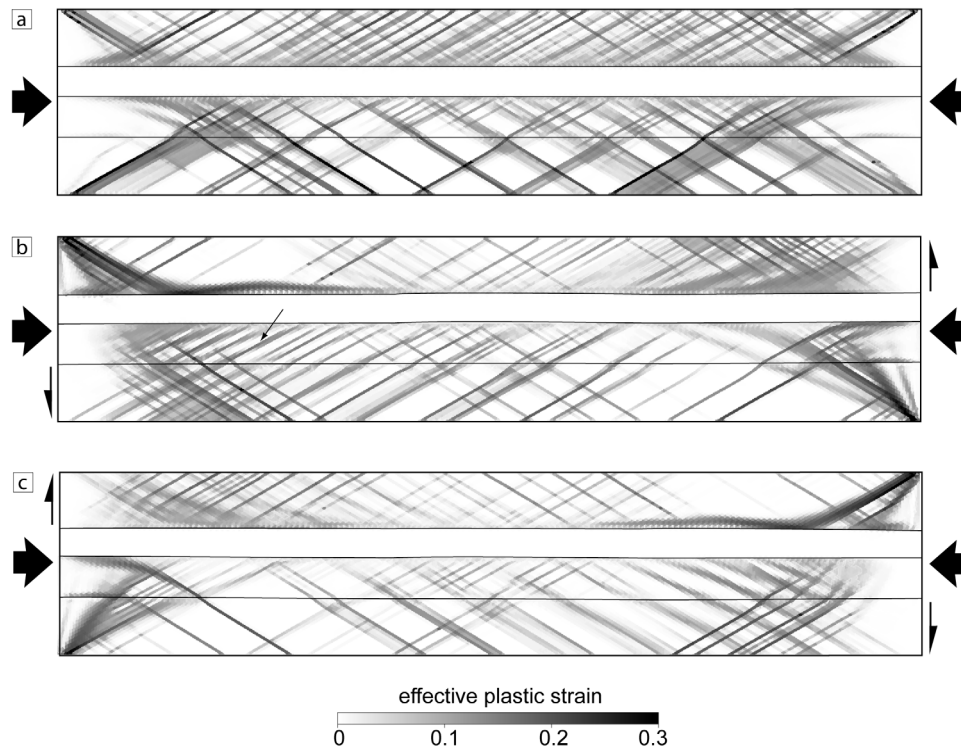


Figure 6. Numerical runs showing the concentration of the effective plastic strain in narrow zones of low strain resembling deformation bands. (a) Simulation with layer-parallel contractional displacement. Bands grow in layers 1, 2 and 4, in nearly orthogonal orientations, as observed in the field. Higher cohesion in layer 3 was found to impede band growth. (b) Addition of counterclockwise shear imposed on the vertical boundaries produces preferential growth of one set of bands as well as twisted ribbons. (c) Addition of clockwise shear facilitates preferential growth of the opposite set of bands.

the degree and kind of cementation of the sandstones of layers 1 to 4. In particular, model input values for Young's modulus were chosen based on the measured tangent Young's modulus variations of the mechanical stratigraphy (Figure 3b), values for cohesion were estimated [Hatheway and Kiersch, 1989] and modeled over the range of plausible values, and friction angles were inferred from standard literature values [e.g., Bolton, 1986; Wibberley *et al.*, 2007].

[33] For the initial numerical run, rock physical and rheological values for layer 1 were assigned for tangent Young's modulus to be $E_1 = 3$ GPa, for Poisson's ratio to be $\nu_1 = 0.3$, the rock density to be $\rho_1 = 2400$ kg/m³, for the cohesion we chose $C_1 = 1$ MPa, and a friction angle of $\phi_1 = 30^\circ$. Layer 2, the layer displaying the prominent deformation band network, was assigned values of $E_2 = 0.9$ GPa, $\nu_2 = 0.25$, $\rho_2 = 2100$ kg/m³, $C_2 = 1$ MPa, and $\phi_2 = 29^\circ$. The calcite cemented and heterogeneous layer 3 has values of $E_3 = 2$ GPa, $\nu_3 = 0.3$, $\rho_3 = 2600$ kg/m³, $C_3 = 20$ MPa, and $\phi_3 = 35^\circ$. Values for layer 4 were chosen to be $E_4 = 2$ GPa, $\nu_4 = 0.3$, $\rho_4 = 2600$ kg/m³, $C_4 = 1$ MPa, and $\phi_4 = 31^\circ$. Results of the parametric study and effects of individual parameters are discussed in section 4.2.

4.2. Model Results

[34] Finite element modeling of layer-parallel compression of the multilayer sequence (Figure 6a and Animation S1 in the auxiliary material) results in the formation of a network of narrow zones of strain localization, whose widths are

controlled by the mesh size assigned to the numerical run.¹ The model agrees well with the deformation bands observed in the exposure of the Orange quarry in terms of both overall angular relations of and between the sets of bands as well as the occurrence of bands within specific layers. The bands in the layer-parallel compression simulation are formed as a synchronous conjugate set. Their dip angles vary between 30° and 40° , similar to band orientations found in the Orange quarry.

[35] The simulated deformation band network geometries of all three layers (Figure 6a) closely resemble the field observations (Figure 3a). In both field and simulations, fewer bands occur in layer 1 relative to the other layers containing bands, i.e., layers 2 and 4. Within layer 2, bands are developed in clusters, whereas in layer 4 they occur evenly and densely spaced. In the simulations, the differences in network geometry between the individual layers with bands were achieved by assigning a small stiffness contrast based on the trends in our mechanical stratigraphy (Figure 3b).

[36] In the layer-parallel compression simulations (Figure 6a), deformation bands are developed within layers 1, 2 and 4. Layer 3 is devoid of bands. From field observations, the calcareous sandstone layer 3 is found to be more heterogeneous, as apparent from variations in calcite cemen-

¹Auxiliary materials are available in the HTML. doi:10.1029/2011JB008365.

tation and grain sizes as well as presence of fossils (Figure 3b). This motivates modeling this layer with higher values for cohesion than the sandstone layers 1, 2 and 4. The increased cohesion was found to impede strain localization. As discussed below, this indicates that layer strength, rather than stiffness, exerts the primary control on whether strain localizes and deformation bands would form in a given layer.

[37] Bands initiate in layers 1 and 4 and with increasing imposed deformation, bands penetrate into layer 2, where they first grow as single bands. Once these single bands display a certain amount of strain in the model, clusters of the same and oppositely dipping bands initiate on top of and next to the older bands (see Animation S1). Such clustering behavior of the bands is also observed in the Orange quarry and is a common stage during the evolution of deformation band damage zones [Aydin and Johnson, 1978; Fossen and Hesthammer, 1997; Shipton et al., 2005]. In the layer-parallel compression simulations this process is observed to happen mutually along both sets of bands.

[38] The geometric similarities between the deformation band pattern of the layer-parallel compression numerical runs and the deformation band network observed in the Orange quarry indicate a good correspondence between the deformation band network and the model. Several differences between observations and the simulations were explored further. The dip of the bands is very homogeneous showing almost no variations as compared to the observed range of band orientations. Also, the bands grow as conjugate sets in the simulations but we observe a sequential growth in the field. These differences were motivation to improve the fit between simulations and observations and to further investigate the controls of the bands and band geometries in our model.

[39] The input values of the representative layer-parallel compression numerical run (Figure 6a) were used as a basis for all following simulations of the parametric study. Parameters were only varied for layer 2, because as the central layer containing deformation bands it is least affected by boundary effects. Results for effects of material constants, rheology, and boundary conditions on the deformation band network geometry are summarized in Table 1 and described below.

[40] As indicated by the layer-parallel compression simulation (Figure 6a), variations of stiffness affect the geometry of the deformation band network. Closer investigation of the effect of varying Young's modulus show that smaller values produce a greater number of bands in the model that are rather evenly distributed throughout the layer but display less plastic shear strain along them. Larger values of Young's modulus result in fewer and more localized bands, each with higher plastic shear strain, as well as a higher concentration of plastic strain along the layer boundaries (see Figure S1). We infer that values of Young's modulus at the lower end of the tested range (of around $E = 0.9$ GPa) are applicable for the geometry of the Orange deformation bands (Table 1) given the generally even distribution of deformation bands with in the outcrop (i.e., layer 2) [Saillet and Wibberley, 2010].

[41] The effects of the parameters of the Drucker-Prager rheology were studied by varying the cohesion and the friction angle. The cohesion in layer 2 was progressively increased up to an order of magnitude above the value of the initial run. As demonstrated for layer 3 in the layer-parallel compression simulations, we find that the cohesion strongly

influences the formation of deformation bands. Higher values of cohesion of $C = 5$ and 10 MPa assigned to layer 2 progressively impeded the formation of the bands up to the point where bands were completely stopped from growing in the model (see auxiliary material). Increased values for cohesion in layer 3 that impeded deformation band growth are related to a variety of properties, including reduced grain size, increased grain angularity and the degree of cementation infilling pore space.

[42] The impact of the friction angle on band formation and orientation was studied by varying it between 20° and 40° . It was found to control the amount of strain on the bands and cause minor changes in the dip angle of the bands (Table 1). Numerical runs with higher friction angle promoted band lock-up at band intersections and low angles promoted very wide, less strongly localized zones of low strain. Modeled band formation during strain hardening or softening was governed by either the initial or final friction angles, depending on how the limit of plastic strain (κ_c) was chosen. When κ_c was reached early during simulations, impacts of the final friction angle were greater on the amount of strain and orientation of the bands, whereas the impact of the initial friction angle was greater when the plastic limit was reached later. Simulations with friction angles around $\sim 30^\circ$ for layer 2 show results for deformation band network geometry closest to the observed pattern in the field.

[43] In the simulations the geometrical setup of our model also affects the geometry of the bands. Changes in layer thickness influence the length of the bands but not their strain magnitude or spacing, which are key factors for band distribution analyses, layer restriction of bands, and displacement-to-length scaling studies. Wolf et al. [2003] attribute band spacing to layer thickness, as observed from their sandbox modeling. Such a relationship is also suggested by Saillet and Wibberley [2010] for the bands spacing in the Orange quarry. Our simulations, however, do not confirm this relationship, perhaps because the welded layer contacts and consistent mechanical properties overshadowed the geological variability within the layered sequence. Further simulations are necessary to explore this interesting topic.

[44] The model length is found to influence the intensity of boundary effects on the deformation band network. Longer models have larger areas unaffected by boundary effects and thus they yield more representative results for band geometries. We also varied the mesh size and found that it governs the band thickness, spacing and number of bands. Due to the increased number of individual cells, a finer mesh decreases the thickness of individual bands and permits a more detailed prediction of band distribution. Additionally, finer mesh sizes produce a higher number of equally distributed bands, as compared to simulations with coarser meshes but same imposed strain.

[45] Layer-parallel shortening affects the magnitude of the strain on the bands and band frequency, whereas misalignment of maximum compression with the layers causes a preferential development of one set of bands, evident in the models by number and thickness of the bands (Figures 6b and 6c). The dip direction of the preferentially developed bands depends on the sense of imposed shear, so that reversing the shear sense creates preferential band growth in the opposite direction (Figures 6b and 6c). Such collective change of orientation of the entire set of bands is consistent with our

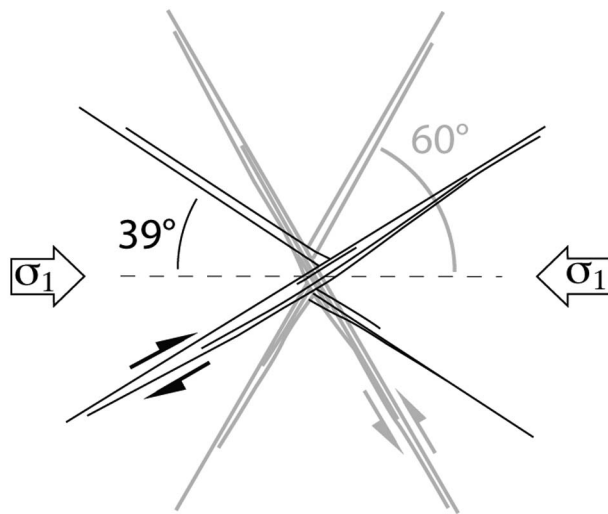


Figure 7. Inclination of deformation bands of the Orange quarry (black) to the maximum compressive stress axis σ_1 , in comparison to sheared compaction bands (gray). Deformation bands (N2, S2) are shown to have a $\sim 39^\circ$ angle toward σ_1 , whereas the sheared compaction bands are shown with an angle of 60° toward the maximum compressive stress.

field observations. The similarities between the numerically recreated band network and the field observations therefore suggest that the multilayer sequence in the outcrop was likely affected by far-field shear. Such shearing boundary conditions may have occurred due to fold limb shear during the history of the folding of the Upper Cretaceous strata. Misalignment of maximum compression also causes progressively decreasing dip angles within a forming band (see arrow in Figures 6b), which, although on a different scale, resembles the twisted ribbon bands observed in the field (Figures 2d and 2e).

5. Implications

[46] The inclination a shear band makes with the axis of maximum compression can be estimated by its relation to friction (ϕ) and dilatancy angles (ψ) [Arthur *et al.*, 1977; Vardoulakis, 1980; Hobbs *et al.*, 1990], where $\alpha = \pi/4 - (\phi - \psi)/4$. Dilatancy describes the change in volume associated with the shear distortion of a granular material [e.g., Vermeer and de Borst, 1984], where positive dilatancy angles are related to volume increase (dilation) and negative values to volume decrease (compaction). A value of $\psi = 0^\circ$, as used in our simulations, combined with a friction angle of $\phi \approx 30^\circ$ result in band inclinations to the maximum compression of $\alpha \approx 37.5^\circ$, consistent with the average field values of the second-generation bands. Because values of $\psi = 0^\circ$ are required in ADELI 2D to achieve band angles of $\sim 38^\circ$, consistent with our field observations, the value of host-rock friction of $\phi = 30^\circ$ is somewhat arbitrary. Given this limitation, a material with a friction angle of $\phi \approx 30^\circ$ that contains bands with inclinations of more than 37.5° requires negative dilatancy angles to represent volume decrease and overall compactional deformation of the deformed rock.

[47] Field and modeled values of the inclination of the deformation bands to the principal axis of compression are both 35° to 40° for set 2 (N2, S2) of the Orange deformation bands. Similar angles to those from bands at the Orange quarry to the axis of maximum compression were measured by Olsson *et al.* [2004] from deformation bands in sandstones of the San Juan basin, New Mexico, and by Ord *et al.* [1991] from biaxial laboratory tests. These orientations are in accord with angles between faults that accommodate frictional sliding. However, this angle appears inconsistent with deformation bands that form as compactional structures at high angles to the maximum compressive stress (Figure 7) [e.g., Olsson, 1999; Rudnicki, 2004]. Furthermore, Eichhubl *et al.* [2010] analyze angular relationships of pure compaction bands, shear-enhanced compaction bands and shear bands to the axes of maximum compression in the Aztec Sandstone. There, several generations of bands are also developed as sequential sets. In particular, reverse-sense shear-enhanced compaction bands are oriented with angles as low as 38° to the general axis of maximum compression. These shear-enhance compaction bands form at similar angles to σ_1 as the deformation bands at the Orange quarry. This finding indicates that band orientations relative to the direction of maximum compression are not unique or diagnostic to the band type. The type of band may not just be indicated by its orientation to σ_1 , but also by different combinations of normal and shear strain, host rock properties, and band internal deformation mechanisms, such as granular flow, cataclasis, or dissolution transfer.

[48] Vermeer [1990] explains such variation in band orientations with varying grain size properties of sandstone. Finer sands are found to produce bands according to the Coulomb orientation, whereas coarser sands tend to show bands according to the Roscoe orientation. Here, the Coulomb orientation, the orientation that a band makes to the normal to maximum compression, θ_C , is related to the friction angle, ϕ , as $\theta_C = 45^\circ + \phi/2$ [e.g., Jaeger and Cook, 1979]. In contrast, the Roscoe orientation relates the orientation that a band makes to the normal to maximum compression, θ_R , to the dilatancy angle, ψ , as $\theta_R = 45^\circ + \psi/2$ [Roscoe, 1970]. The Coulomb orientation is consistent with the overall band angles of deformation bands, as found in the Orange quarry, while the Roscoe orientation is consistent with typical angles of shear-enhanced compactional bands. Furthermore, this finding explains the preferred occurrence of compactional bands in coarse grained, well sorted, and highly porous sands and their absence in finer sandstones [e.g., Mollema and Antonellini, 1996], whereas deformation bands can grow with Coulomb angles in finer grained, less mature sandstones.

[49] The deformation observed in the Orange quarry is, in general, evenly distributed throughout the entire layer [Saillet and Wibberley, 2010]. Although we only focus on the outcrop-scale processes and do not directly account for a propagating fault at depth in the simulations, we attribute this homogeneity of deformation band distribution to the nearly layer-parallel compression associated with the flexure of the multilayer sequence over a blind thrust (Figure 1b), similar to other settings of thrust fault-related folds. The deformation bands at the Orange quarry do not directly accompany a propagating fault, pointing out that such even deformation band distribution is unlike the highly clustered deformation band distribution in relatively narrow process

zones surrounding faults that impinge on or dissect sandstone units, such as the bands predating or accompanying normal faults at the classic deformation band site near Goblin Valley, Utah [Aydin, 1978, Aydin and Johnson, 1978]. We therefore suggest that wide zones of even or distributed deformation band distribution predominantly occur in structural settings where sandstone layers are deformed by regional layer-parallel shortening rather than in settings where the combination of rock properties and far-field stress state lead to localization of band networks, consistent with preliminary results from other locations [e.g., Soliva *et al.*, 2011].

[50] Results of our field work and simulations extend the knowledge about deformation bands in the Orange quarry, which allows putting the observed deformation in the quarry into a regional geologic context. The Bassin du Sud-Est is characterized by gentle folding of the surface strata caused by faulting at depth. The quarry exposure is located near the hinge of the Orange anticline, which formed over an upward propagating blind thrust fault (Figure 1b) that has been related to Pyrenean shortening from the south [Arthaud and Séguret, 1981; Tempier, 1987; Séguret *et al.*, 1996; Sanchis and Seranne, 2000]. Correspondingly, the layer-parallel compression that produced the several sets of deformation bands at Orange quarry is likely related to the Pyrenean shortening. Since the folding is related to the upward propagation of the thrust fault at depth, the fold hinge of the above anticline should also change in location with time. We infer from our simulations (Figures 6a, 6b, and 6c) that the rocks of the Orange exposure might have been gently rotated along both sides of the hinge and therefore experienced a modest change of the shear sense, leading to opposite sets of reverse-sense bands that formed sequentially.

6. Conclusions

[51] The controls on deformation band geometries were investigated by studying deformation bands formed in a multilayer sequence of Cretaceous sandstones and limestones in the Orange quarry, Bassin du Sud-Est, France. Four sequential sets having reverse senses of shearing offset are found to form most prominently within layer 2 of the multilayer stack, terminating against the overlying calcite cemented sandstone layer but propagating into the subjacent layer. Detailed field mapping refines the sequence and mechanics of the bands and was the basis for successfully simulating their growth within this stack by two-dimensional finite element simulations.

[52] While previous work focused on the prominent multiple-strand cataclastic bands in the quarry, we identified an earlier set of reverse-sense deformation bands that display similar characteristics but consist of mainly single strands. These early bands are overprinted by the more prominent second generation bands. Both generations of bands have similar orientations to bedding, implying that they formed during the same episode of layer-parallel contraction. In addition, the bands formed in sequential parallel sets, rather than in mutually crosscutting conjugate sets as suggested previously.

[53] Deformation band growth was modeled in the multilayer sequence by using ADELI 2D. Layer properties were idealized as Drucker-Prager materials having specified values of friction angle, cohesion, and stiffness. Application of a

layer-parallel shortening displacement led to deformation bands forming in the sandstone layers (layers 1, 2 and 4) and not in the calcite cemented sandstone layer 3, consistent with the field observations. The results indicate that layer strength, rather than stiffness, control the formation of deformation bands. In addition, we relate band angles to rheological and petrophysical rock properties and associated yielding behavior.

[54] While conjugate sets are formed by imposing layer-parallel shortening, preferential growths of bands was achieved by imposing shear onto the model. The preferential growth of bands in sequential parallel sets in Orange quarry may be related to folding of the multilayer sequence above a blind thrust fault. The results are applicable to the interpretation and prediction of deformation bands in multilayer sequences in other areas of contractional tectonics.

[55] **Acknowledgments.** We thank Haakon Fossen and an anonymous reviewer for their thoughtful comments that sharpened the final paper. We also thank Philippe Vernant for his alacrity and patience in helping to set up ADELI 2D on a Mac, and Philippe Steer for providing graphics software to visualize the modeling results as well as providing the Schmidt hammer. Iona Summerson is thanked for her assistance in the field. This work was supported by a grant from NASA's Planetary Geology and Geophysics Program.

References

- Arthaud, F., and A. Séguret (1981), Les structures pyrénéennes du Languedoc et du Golfe du Lion (Sud de la France), *Bull. Soc. Geol. Fr.*, *XXIII*, 51–63.
- Arthur, J. R. F., T. Dunstan, Q. A. J. Al-Ani, and A. Assadi (1977), Plastic deformation and failure of granular media, *Geotechnique*, *27*, 53–74, doi:10.1680/geot.1977.27.1.53.
- Aufmuth, R. E. (1973), A systematic determination of engineering criteria for rock, *Bull. Assoc. Eng. Geol.*, *11*, 235–245.
- Aydin, A. (1978), Small faults formed as deformation bands in sandstone, *Pure Appl. Geophys.*, *116*, 913–930, doi:10.1007/BF00876546.
- Aydin, A. (2009), ISRM suggested method for determination of the Schmidt hammer rebound hardness: Revised version, *Int. J. Rock Mech. Min. Sci.*, *46*, 627–634, doi:10.1016/j.ijrmms.2008.01.020.
- Aydin, A., and A. M. Johnson (1978), Development of faults as zones of deformation bands and as slip surfaces in sandstone, *Pure Appl. Geophys.*, *116*, 931–942, doi:10.1007/BF00876547.
- Baud, P., E. Klein, and T.-f. Wong (2004), Compaction localization in porous sandstones: Spatial evolution of damage and acoustic emission activity, *J. Struct. Geol.*, *26*, 603–624, doi:10.1016/j.jsg.2003.09.002.
- Bolton, M. D. (1986), The strength and dilatancy of sands, *Geotechnique*, *36*, 65–78, doi:10.1680/geot.1986.36.1.65.
- Cashman, S., and K. Cashman (2000), Cataclasis and deformation-band formation in unconsolidated marine terrace sand, Humboldt County California, *Geology*, *28*, 111–114, doi:10.1130/0091-7613(2000)28<111:CADFIU>2.0.CO;2.
- Chéry, J. (2001), Core complexes mechanics: From Corinth Gulf to Snake Range, *Geology*, *29*, 439–442, doi:10.1130/0091-7613(2001)029<0439:CCMFTG>2.0.CO;2.
- Chéry, J., M. D. Zoback, and S. Hickman (2004), A mechanical model of the San Andreas fault and SAFOD pilot hole stress measurements, *Geophys. Res. Lett.*, *31*, L15S13, doi:10.1029/2004GL019521.
- Davis, G. H. (1999), Structural geology of the Colorado Plateau region of southern Utah, with special emphasis on deformation bands, *Spec. Pap. Geol. Soc. Am.*, *342*, 157 pp., doi:10.1130/0-8137-2342-6.1.
- Davis, R. O., and A. P. S. Selvadurai (2002), *Plasticity and Geomechanics*, Cambridge Univ. Press, Cambridge, U. K., doi:10.1017/CBO9780511614958.
- Davis, G. H., A. P. Bump, P. E. García, and S. G. Ahlgren (2000), Conjugate Riedel deformation band shear zones, *J. Struct. Geol.*, *22*, 169–190, doi:10.1016/S0191-8141(99)00140-6.
- Du Bernard, X., P. Eichhbul, and A. Aydin (2002a), Dilation bands: A new form of localized failure in granular media, *Geophys. Res. Lett.*, *29*(24), 2176, doi:10.1029/2002GL015966.
- Du Bernard, X., P. Labaume, C. Darcel, P. Davy, and O. Bour (2002b), Cataclastic slip band distribution in normal fault damage zones, Nubian

- sandstones, Suez rift, *J. Geophys. Res.*, 107(B7), 2141, doi:10.1029/2001JB000493.
- Eichhubl, P., J. N. Hooker, and S. E. Laubach (2010), Pure and shear-enhanced compaction bands in Aztec sandstone, *J. Struct. Geol.*, 32, 1873–1886, doi:10.1016/j.jsg.2010.02.004.
- Ford, M., and U. Stahel (1995), The geometry of a deformed carbonate slope–basin transition: The Ventoux–Lure fault zone, SE France, *Tectonics*, 14, 1393–1410, doi:10.1029/95TC02522.
- Fossen, H., and A. Bale (2007), Deformation bands and their influence on fluid flow, *AAPG Bull.*, 91, 1685–1700, doi:10.1306/07300706146.
- Fossen, H., and J. Hesthammer (1997), Geometric analysis and scaling relations of deformation bands in porous sandstone, *J. Struct. Geol.*, 19, 1479–1493, doi:10.1016/S0191-8141(97)00075-8.
- Fossen, H., R. A. Schulz, Z. K. Shipton, and K. Mair (2007), Deformation bands in sandstone: A review, *J. Geol. Soc.*, 164, 755–769, doi:10.1144/0016-76492006-036.
- Freund, R. (1970), Rotation of strike-slip faults in Sistan, south Iran, *J. Geol.*, 78, 188–200, doi:10.1086/627500.
- Grueschow, E., and J. W. Rudnicki (2005), Elliptic yield cap constitutive modeling for high porosity sandstone, *Int. J. Solids Struct.*, 42, 4574–4587, doi:10.1016/j.ijsolstr.2005.02.001.
- Hassani, R., and J. Chéry (1996), Anelasticity explains topography associated with Basin and Range normal faulting, *Geology*, 24, 1095–1098, doi:10.1130/0091-7613(1996)024<1095:AETAWB>2.3.CO;2.
- Hatheway, A. W., and G. A. Kiersch (1989), Engineering properties of rock, in *Practical Handbook of Physical Properties of Rocks and Minerals*, edited by R. S. Carmichael, pp. 672–715, CRC Press, Boca Raton, Fla.
- Hesthammer, J., and H. Fossen (2001), Structural core analysis from the Gullfaks area, northern North Sea, *Mar. Pet. Geol.*, 18, 411–439, doi:10.1016/S0264-8172(00)00668-4.
- Hobbs, B. E., H.-B. Millheus, and A. Ord (1990), Instability, softening and localization of deformation, *Geol. Soc. Spec. Publ.*, 54, 143–165, doi:10.1144/GSL.SP.1990.054.01.15.
- Jaeger, J. C., and N. G. W. Cook (1979), *Fundamentals of Rock Mechanics*, Chapman and Hall, London, doi:10.1017/CBO9780511735349.
- Johnson, A. M. (1995), Orientations of faults determined by premonitory shear zones, *Tectonophysics*, 247, 161–238, doi:10.1016/0040-1951(95)00002-5.
- Kamer, S. L., J. S. Chester, F. M. Chester, A. K. Kronenberg, and A. Hajash Jr. (2005), Laboratory deformation of granular quartz sand: Implications for the burial of clastic rocks, *AAPG Bull.*, 89, 603–625, doi:10.1306/12200404010.
- Klimczak, C. (2011), Processes of progressive deformation with applications to faulting, jointing, and fluid flow, Ph.D. dissertation, 241 pp., Univ. of Nevada, Reno, Reno.
- Kolyukhin, D., S. Schueller, M. S. Espedal, and H. Fossen (2010), Deformation band populations in fault damage zone—Impact on fluid flow, *Comput. Geosci.*, 14, 231–248, doi:10.1007/s10596-009-9148-8.
- Lothe, A. E., R. H. Gabrielsen, N. Bjørnevoll-Hagen, and B. T. Larsen (2002), An experimental study of the texture of deformation bands; effects on the porosity and permeability of sandstones, *Petrol. Geosci.*, 8, 195–207, doi:10.1144/petgeo.8.3.195.
- Mair, K., I. Main, and S. Elphick (2000), Sequential growth of deformation bands in the laboratory, *J. Struct. Geol.*, 22, 25–42, doi:10.1016/S0191-8141(99)00124-8.
- Marshak, S., P. A. Geiser, W. Alvarez, and T. Engelder (1982), Mesoscopic fault array of the northern Umbrian Apennine fold belt, Italy: Geometry of conjugate shear by pressure-solution slip, *Geol. Soc. Am. Bull.*, 93, 1013–1022, doi:10.1130/0016-7606(1982)93<1013:MFAOTN>2.0.CO;2.
- Mollema, P. N., and M. A. Antonellini (1996), Compaction bands: A structural analog for anti-mode I cracks in aeolian sandstone, *Tectonophysics*, 267, 209–228, doi:10.1016/S0040-1951(96)00098-4.
- Okubo, C. H., and R. A. Schultz (2005), Evolution of damage zone geometry and intensity in porous sandstone: Insight gained from strain energy density, *J. Geol. Soc.*, 162, 939–949, doi:10.1144/0016-764904-148.
- Okubo, C. H., and R. A. Schultz (2006), Near-tip stress rotation and the development of deformation band stepover geometries in mode II, *Geol. Soc. Am. Bull.*, 118, 343–348, doi:10.1130/B25820.1.
- Olsson, W. A. (1999), Theoretical and experimental investigation of compaction bands in porous rock, *J. Geophys. Res.*, 104, 7219–7228, doi:10.1029/1998JB900120.
- Olsson, W. A., J. C. Lorenz, and S. P. Cooper (2004), A mechanical model for multiply oriented conjugate deformation bands, *J. Struct. Geol.*, 26, 325–338, doi:10.1016/S0191-8141(03)00101-9.
- Ord, A., I. Vardoulakis, and R. Kajewski (1991), Shear band formation in Gosford Sandstone, *Int. J. Rock Mech. Min. Sci.*, 28, 397–409, doi:10.1016/0148-9062(91)90078-Z.
- Provost, A.-S., J. Chéry, and R. Hassani (2003), 3D mechanical modeling of the GPS velocity field along the North Anatolian Fault, *Earth Planet. Sci. Lett.*, 209, 361–377, doi:10.1016/S0012-821X(03)00099-2.
- Roscoe, K. H. (1970), The influence of strains in soil mechanics, *Geotechnique*, 20, 129–170, doi:10.1680/geot.1970.20.2.129.
- Roure, F., J.-P. Brun, B. Colletta, and R. Vially (1994), Multiphase extensional structures, fault reactivation and petroleum plays in the Alpine foreland of southeastern France, in *Hydrocarbon and Petroleum of France, Spec. Publ. Eur. Assoc. Pet. Geol.*, vol. 4, edited by A. Mascle, pp. 245–267, Springer-Verlag, Berlin.
- Rudnicki, J. W. (1977), The inception of faulting in a rock mass with a weakened zone, *J. Geophys. Res.*, 82, 844–854, doi:10.1029/JB082i005p00844.
- Rudnicki, J. W. (2004), Shear and compaction band formation on an elliptic yield cap, *J. Geophys. Res.*, 109, B03402, doi:10.1029/2003JB002633.
- Saada, A. S., L. Liang, J. L. Figueroa, and C. T. Cope (1999), Bifurcation and shear band propagation in sands, *Geotechnique*, 49, 367–385, doi:10.1680/geot.1999.49.3.367.
- Saillet, E., and C. A. J. Wibberley (2010), Evolution of cataclastic faulting in high-porosity sandstone, Bassin du Sud-Est, Provence, France, *J. Struct. Geol.*, 32, 1590–1608, doi:10.1016/j.jsg.2010.02.007.
- Sanchis, E., and M. Seranne (2000), Structural style and tectonic evolution of a polyphase extensional basin of the Gulf of Lion passive margin: The Tertiary Alès basin, southern France, *Tectonophysics*, 322, 219–242, doi:10.1016/S0040-1951(00)00097-4.
- Schultz, R. A., and C. M. Balasko (2003), Growth of deformation bands into echelon and ladder geometries, *Geophys. Res. Lett.*, 30(20), 2033, doi:10.1029/2003GL018449.
- Schultz, R. A., and R. Siddharthan (2005), A general framework for the occurrence and faulting of deformation bands in porous granular rocks, *Tectonophysics*, 411, 1–18, doi:10.1016/j.tecto.2005.07.008.
- Schultz, R. A., C. H. Okubo, and H. Fossen (2010), Porosity and grain size controls on compaction band formation in Jurassic Navajo Sandstone, *Geophys. Res. Lett.*, 37, L22306, doi:10.1029/2010GL044909.
- Schultz-Ela, D. D., and P. Walsh (2002), Modeling of grabens extending above evaporates in Canyonlands National Park, Utah, *J. Struct. Geol.*, 24, 247–275, doi:10.1016/S0191-8141(01)00066-9.
- Séguret, M., A. Benedicto, and M. Séranne (1996), Gard Rhodanien, reconnaissance géologique. Analyse et interprétation structurale préliminaire du profil sismique FSH (82 SE 4B), *Rapp. ANDRA, BRP 1 UCB 96-001A*, Bur. de Rech. Géol. et Min., Paris.
- Séranne, M., A. Benedicto, P. Labaume, C. Truffert, and G. Pascal (1995), Structural style and evolution of the Gulf of Lion Oligo-Miocene rifting: Role of the Pyrenean orogeny, *Mar. Pet. Geol.*, 12, 809–820, doi:10.1016/0264-8172(95)98849-Z.
- Shipton, Z. K., and P. A. Cowie (2001), Damage zone and slip-surface evolution over μm to km scales in high-porosity Navajo Sandstone, Utah, *J. Struct. Geol.*, 23, 1825–1844, doi:10.1016/S0191-8141(01)00035-9.
- Shipton, Z. K., and P. A. Cowie (2003), A conceptual model for the origin of fault damage zone structures in high-porosity sandstone, *J. Struct. Geol.*, 25, 333–344, doi:10.1016/S0191-8141(02)00037-8.
- Shipton, Z. K., J. P. Evans, K. Robeson, C. B. Forster, and S. Snelgrove (2002), Structural heterogeneity and permeability in faulted eolian sandstone: Implications for subsurface modelling of faults, *AAPG Bull.*, 86, 863–883.
- Shipton, Z. K., J. P. Evans, and L. B. Thompson (2005), The geometry and thickness of deformation-band fault core and its influence on sealing characteristics of deformation-band fault zones, in *Faults, Fluid Flow, and Petroleum Traps*, edited by R. Sorkhabi and Y. Tsuji, *AAPG Mem.*, 85, 181–195.
- Soliva, R., R. A. Schultz, G. Ballas, A. Taboada, E. Saillet, C. A. Wibberley, and A. Benedicto (2011), The relationship between deformation band properties, tectonic regime and burial in porous sandstone, *Geophys. Res. Abstr.*, 13, EGU/2011-6377.
- Stanchits, S., J. Fortin, Y. Gueguen, and G. Dresen (2009), Initiation and propagation of compaction bands in dry and wet Bentheim Sandstone, *Pure Appl. Geophys.*, 166, 843–868, doi:10.1007/s00024-009-0478-1.
- Sternlof, K. R., M. Karimi-Fard, D. D. Pollard, and L. J. Durlofsky (2006), Flow and transport effects of compaction bands in sandstone at scales relevant to aquifer and reservoir management, *Water Resour. Res.*, 42, W07425, doi:10.1029/2005WR004664.
- Suppe, J. (1983), Geometry and kinematics of fault-bend-folding, *Am. J. Sci.*, 283, 684–721, doi:10.2475/ajs.283.7.684.
- Suppe, J., and D. A. Medwedeff (1990), Geometry and kinematics of fault propagation-folding, *Eclogae Geol. Helv.*, 83, 409–454.
- Tempier, C. (1987), Modèle nouveau de mise en place des structures provençales, *Bull. Soc. Geol. Fr.*, 8, 533–540.

- Vardoulakis, I. G. (1980), Shear band inclination and shear modulus of sand in biaxial tests, *Int. J. Numer. Anal. Methods Geomech.*, **4**, 103–119, doi:10.1002/nag.1610040202.
- Vermeer, P. A. (1990), The orientation of shear bands in biaxial tests, *Geotechnique*, **40**, 223–236, doi:10.1680/geot.1990.40.2.223.
- Vermeer, P. A., and R. de Borst (1984), Non-associated plasticity for soils, concrete, and rock, *Heron*, **29**, 3–64.
- Vernant, P., and J. Chéry (2006), Mechanical modelling of oblique convergence in the Zagros, Iran, *Geophys. J. Int.*, **165**, 991–1002, doi:10.1111/j.1365-246X.2006.02900.x.
- Wang, J., Z.-R. Ye, and J.-K. He (2008), Three-dimensional mechanical modeling of large-scale crustal deformation in China constrained by the GPS velocity field, *Tectonophysics*, **446**, 51–60, doi:10.1016/j.tecto.2007.11.006.
- Wibberley, C. A. J., J.-P. Petit, and T. Rives (2000), Mechanics of cataclastic ‘deformation band’ faulting in high-porosity sandstone, Provence, *C. R. Acad. Sci.*, **331**, 419–425.
- Wibberley, C. A. J., J.-P. Petit, and T. Rives (2007), The mechanics of fault distribution and localization in high-porosity sands, Provence, France, *Geol. Soc. Spec. Publ.*, **289**, 19–46, doi:10.1144/SP289.3.
- Wolf, H., D. König, and T. Triantafyllidis (2003), Experimental investigation of shear band patterns in granular material, *J. Struct. Geol.*, **25**, 1229–1240, doi:10.1016/S0191-8141(02)00163-3.
- Wong, T.-f., and P. Baud (1999), Mechanical compaction of porous sandstone, *Oil Gas Sci. Technol.*, **54**, 715–727, doi:10.2516/ogst:1999061.
- Zhang, J., T.-f. Wong, and D. M. Davis (1990), Micromechanics of pressure-induced grain crushing in porous rocks, *J. Geophys. Res.*, **95**, 341–352, doi:10.1029/JB095iB01p00341.

J. Chéry and R. Soliva, Géosciences, UMR 5243-CC60, Université Montpellier 2, place E. Bataillon, F-34095 Montpellier CEDEX 05, France.
 C. Klimczak, Department of Terrestrial Magnetism, Carnegie Institution of Washington, 5241 Broad Branch Rd., NW, Washington, DC 20015-1305, USA. (cklimczak@ciw.edu)
 R. A. Schultz, ConocoPhillips, Subsurface Technology, 600 North Dairy Ashford, Houston, TX 77079, USA. (richard.a.schultz@conocophillips.com)